

Characterization of Multiple 3D LiDARs for Localization and Mapping using Normal Distributions Transform

Alexander Carballo^{1,4}
Yuki Kitsukawa^{2,4}

Abraham Monrroy^{2,4}
Eijiro Takeuchi^{2,4}

David Wong^{1,4}
Shinpei Kato^{3,4,5}

Patiphon Narksri^{2,4}

Jacob Lambert^{2,4}
Kazuya Takeda^{1,2,4}

Abstract—In this work, we present a detailed comparison of ten different 3D LiDAR sensors, covering a range of manufacturers, models, and laser configurations, for the tasks of mapping and vehicle localization, using as common reference the Normal Distributions Transform (NDT) algorithm implemented in the self-driving open source platform Autoware. LiDAR data used in this study is a subset of our LiDAR Benchmarking and Reference (LIBRE) dataset, captured independently from each sensor, from a vehicle driven on public urban roads multiple times, at different times of the day. In this study, we analyze the performance and characteristics of each LiDAR for the tasks of (1) 3D mapping including an assessment map quality based on mean map entropy, and (2) 6-DOF localization using a ground truth reference map.

Index Terms—3D LiDAR, localization, mapping, normal distributions transform, LIBRE dataset

I. INTRODUCTION

State-of-the-art vehicle navigation, in particular localization and obstacle negotiation, cannot be conceived without referring to LiDARs (*Light Detection And Ranging*, sometimes *Light Imaging Detection And Ranging* for the image-like resolution of modern 3D sensors). Ever since the first implementations of SLAM (simultaneous localization and mapping) for robotics[11] and practical demonstrations on vehicles[12], LRF (laser range finders) and LiDARs have had a major role to realize high accuracy 2D occupancy maps and 3D pointcloud maps. Current MMS (mobile mapping systems) employ several LiDARs together with IMUs, cameras, GNSS, odometry, to capture with the highest fidelity all the environments elements involved in driving.

The rapid developments in the field of intelligent transport systems (ITS) have created a large demand for LiDARs for obstacle negotiation, navigation, sensing in intelligent highways, and so on. Each operational design domain (ODD) defines several key requirements expected from LiDARs: measurement range, measurement accuracy, repeatability,

¹Institute of Innovation for Future Society, Nagoya University, Furo-cho, Chikusa-ku, Nagoya 464-8601, Japan.

²Graduate School of Informatics, Nagoya University, Furo-cho, Chikusa-ku, Nagoya 464-8603, Japan.

³Graduate School of Information Science and Technology, University of Tokyo, 7-3-1 Hongo, Bunkyo-ku, Tokyo, 113-0033, Japan.

⁴TierIV Inc., Nagoya University Open Innovation Center, 1-3, Mei-eki 1-chome, Nakamura-Ward, Nagoya, 450-6610, Japan.

⁵The Autoware Foundation, 3-22-5, Hongo, Bunkyo-ku, Tokyo, 113-0033, Japan.

Email:alexander@g.sp.m.is.nagoya-u.ac.jp,
abraham.monrroy@tier4.jp, david.wong@tier4.jp,
narksri.patiphon@g.sp.m.is.nagoya-u.ac.jp,
jacob.lambert@g.sp.m.is.nagoya-u.ac.jp,
yuki.kitsukawa@tier4.jp, takeuchi@g.sp.m.is.nagoya-u.ac.jp,
shinpei@is.s.u-tokyo.ac.jp, kazuya.takeda@nagoya-u.jp



Fig. 1: Instrumented vehicle used to capture dynamic traffic data in the LIBRE dataset and sensors used in this study.

point density, scanning speed, configurability, wavelengths, robustness to environmental changes, sensing on adverse weather, small form factors, and costs. As such, a large number of LiDAR manufacturers have emerged in recent years introducing new technologies to address different needs[13]. With so many different manufacturers and technologies becoming available, it is necessary to properly assess the characteristics and performance of each device. Furthermore, with LiDAR costs still remaining high, it can be difficult to select the best LiDAR in terms of cost to performance.

We released the LIBRE dataset covering multiple 3D LiDARs[14], [15]. It features 12 LiDARs, each one a different model from diverse manufacturers, includes data from four different environments and configurations: *dynamic traffic* which corresponds to traffic scenes captured from a vehicle driving on public urban roads around Nagoya University; *static targets* related to objects (reflective targets, black car and mannequins) placed at known controlled distances, and measured from a fixed position; *adverse weather* consisting on static objects placed at a fix location and measured from a moving vehicle while exposed to adverse conditions (fog, rain, strong light); and *indirect interference* in which dynamic traffic objects are measured from a fixed position by multiple LiDARs simultaneously and exposed to indirect interference conditions. Our dataset also includes ground truth 3D pointcloud maps and vector maps (HD maps)

	Velodyne						Hesai		Ouster	RoboSense
										
	VLS-128AP* [1]	VLS-128* [2]	HDL-64S2 [3]	HDL-32E [4]	VLP-32C [5]	VLP-16 [6]	Pandar-64 [7]	Pandar-40p [8]	OS1-64 [9]	RS-Lidar32 [10]
Channels	128	128	64	32	32	16	64	40	64	32
FPS[Hz]	5-20	5-20	5-20	5-20	5-20	5-20	10,20	10,20	10,20	5,10,20
Precision[m]	± 0.03	± 0.03	$\pm 0.02^a$	± 0.02	± 0.03	± 0.03	$\pm 0.02^c$	$\pm 0.02^c$	$\pm 0.03^d$	$\pm 0.03^c$
Max.Range[m]	245	300	120	100	200	100	200	200	120	200
Min.Range[m]			3	2	1	1	0.3	0.3	0.8	0.4
vFOV[deg]	40	40	26.9	41.33	40	30	40	40	33.2	40
vRes[deg]	0.11 ^b	0.11 ^b	0.33 ^a	1.33	0.33 ^b	2.0	0.167 ^b	0.33 ^b	0.53	0.33 ^b
λ [nm]	903	903	903	903	903	903	905	905	850	905
ϕ [mm]	165.5	165.5	223.5	85.3	103	103.3	116	116	85	114
Weight(kg)	3.5	3.5	13.5	1.0	0.925	0.830	1.52	1.52	0.425	1.17
Pointcloud fields from driver	$x, y, z,$ intensity, ring, timestamp	$x, y, z,$ intensity, ring, timestamp	$x, y, z,$ intensity, ring	$x, y, z,$ intensity, ring	$x, y, z,$ intensity, ring	$x, y, z,$ intensity, ring	$x, y, z,$ intensity, timestamp, ring	$x, y, z,$ intensity, timestamp, ring	$x, y, z,$ timestamp, intensity, reflectivity, ring	$x, y, z,$ intensity

TABLE I: LiDARs tested in this study, by manufacturer and number of channels (rings)¹. Acronyms are frame rate (FPS), vertical field-of-view (vFOV), vertical resolution (vRes), laser wavelength (λ), and diameter ϕ . ^aVelodyne states HDL-64S2 accuracy is $\pm 2cm$ for 80% of channels, and $\pm 5cm$ for the remaining; vRes for $+2^\circ..-8.33^\circ$ is $1/3^\circ$ and for $-8.83^\circ..-24.33^\circ$ is $1/2^\circ$. ^bMinimum (or finest) resolution, as these sensors have variable angle difference between beams. ^cHesai and RoboSense state that accuracy for $0.3m..0.5m$ is $\pm 0.05m$, then $\pm 0.02m$ from $0.5m..200m$. ^dOuster states accuracy for $0.8m..2m$ is $\pm 0.03m$, for $2m..20m$ is $\pm 0.015m$, for $20m..60m$ is $\pm 0.03m$, and over $60m$ is $\pm 0.10m$. *Velodyne VLS-128 initial release (63-9480 Rev-3) and the latest Velodyne VLS-128 Alpha Prime (63-9679 Rev-1).

created by a professional mobile mapping system (MMS).

Using the dynamic traffic data of our LIBRE dataset, this study focuses on analyzing the characteristics of ten 3D LiDARs for vehicle localization and mapping, considering the LiDAR pointcloud data alone, this is, without assistance of any other navigation and dead reckoning systems such as IMU, GNSS, odometry, or vehicle speed. To the best of our knowledge, this is the first work studying so many LiDARs for vehicle navigation, covering a range of manufacturers, models, and laser configurations (the sensors are listed in Table I). To define a common ground for comparison, we use the Normal Distributions Transform (NDT)[16], [17], [18] in the self-driving open source platform Autoware[19] (see also Kato *et al.*[20]).

The contributions of this work are summarized as follows:

- A unique study of the properties for multiple 3D LiDARs for creation of 3D maps and 6-DOF localization.
- Evaluation of 3D map quality using the mean map entropy (MME) and mean plane variance (MPV) scores for each LiDAR.

This paper is structured as follows: Section II revisits NDT scan matching and its properties. Section III describes the dynamic traffic data and experimental procedures in this study. Sections IV and V discuss the actual result for mapping localization and localization. Finally, this paper is concluded in Section VI.

¹All sensor images¹ not to scale and copyright owned by their respective manufacturers.

II. NORMAL DISTRIBUTIONS TRANSFORM

A. NDT Scan Matching

The Normal Distributions Transform (NDT) scan matching method is attributed to Biber *et al.*[21]. In NDT, the reference scan (pointcloud) is divided into uniform 3D grid, and each cell (voxel) keeps the mean and distribution of the sub-pointcloud assigned to it, thus the ND voxels represent normal distributions.

Following the notation by Takeuchi *et al.*[16], the reference pointcloud (map or model) M is a vector of M points $\mathbf{x}_i = \langle x_i, y_i, z_i \rangle^T$ with $i \in [1..M]$, and x_k is the k -th ND voxel with M_k points. The k -th ND voxel mean \mathbf{p}_k and covariance matrix Σ_k are given by Eq. 1.

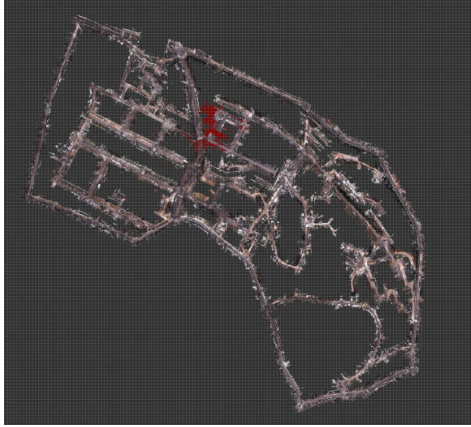
$$\begin{aligned} \mathbf{p}_k &= \frac{1}{M_k} \sum_{i=1}^{M_k} \mathbf{x}_{ki} \\ \Sigma_k &= \frac{1}{M_k} \sum_{i=1}^{M_k} (\mathbf{x}_{ki} - \mathbf{p}_k)(\mathbf{x}_{ki} - \mathbf{p}_k)^T \end{aligned} \quad (1)$$

Given an input scan (pointcloud) X with N points, \mathbf{x}_i with $i \in [1..N]$, the 3D coordinate transformation of X into M is achieved by $\mathbf{x}'_i = \mathbf{R}\mathbf{x}_i + \mathbf{t}'$, with \mathbf{R} the rotation matrix and \mathbf{t}' the translation vector. Thus, the pose transformation

²Google map is available at <https://drive.google.com/open?id=1fFja7B29xmidldvJWPWLKSK0UCrXhy47N&hl=en&z=17>



(a)



(b)

Fig. 2: Map of the dynamic environment included in the dataset: (a) general map², trajectory colored in red corresponds to the complete drive starting at location marked with , and ending at location marked with . Trajectory colored in blue with starting location marked with  corresponds to route A, yellow trajectory with start location marked with  is route B, and trajectory colored in green with starting location marked with  is route C. (b) is the ground truth pointcloud map (grid cell size 10 m) created by a MMS.

parameters (translation and rotation) to estimate are $\mathbf{t} = \langle t_x, t_y, t_z, t_{roll}, t_{pitch}, t_{yaw} \rangle$. Evaluation of fitness between the transformed input cloud $\bar{\mathbf{X}}$ using the parameters \mathbf{t} , and the reference map \mathbf{M} , represented as ND voxels, is done with Eq. 2.

$$E(\mathbf{X}, \mathbf{t}) = \sum_i^N \exp \frac{-(\mathbf{x}'_i - \mathbf{p}_i)^T \Sigma_i^{-1} (\mathbf{x}'_i - \mathbf{p}_i)}{2} \quad (2)$$

A high value of $E(\mathbf{X}, \mathbf{t})$ means both the input cloud and the reference map are well aligned. Newton's nonlinear function optimization is utilized to find \mathbf{t} such that $E(\mathbf{X}, \mathbf{t})$ is maximized. Therefore, we minimize the function $f(\mathbf{t}) = -E(\mathbf{X}, \mathbf{t})$. Parameters vector \mathbf{t} is updated using Eq. 3.

$$\mathbf{t}_{new} = \mathbf{t} - \mathbf{H}^{-1} \mathbf{g} \quad (3)$$

where \mathbf{g} and \mathbf{H} are the partial differential and second order partial differential of the optimizing function f . Details

of the derivation of these values are given in [16], the work by Magnusson[18] includes a very derivation. Magnusson *et al.*[17] and Sobreira *et al.*[22] present detailed comparisons of performance of NDT versus the Iterative Closest Point (ICP) algorithm and others.

B. NDT Evaluation Metrics

1) *Iteration*: Iteration corresponds to the number of cycles (and therefore processing time) of the Newton's iterative method until achieving matching convergence. If the initial guess for the transformation parameters \mathbf{t} is close enough to the actual transformation, then the number of iterations is small.

2) *Fitness Score*: Fitness Score is the degree of correspondence between two scans, obtained by the average sum of distances between closest points. When this score is small then correspondence between pointclouds is high. However, if the reference cloud lacks areas which are part of the input cloud, the distance between closest neighbors increases and so this score.

3) *Transformation Probability*: Transformation Probability, although strictly speaking not a probability, is the score of one point, obtained by dividing the fitness score by the number of points N of the input scan.

C. NDT Precision and Performance Factors

1) *Input Cloud Down-sampling*: The input cloud of conventional LiDARs may consist on tens to hundreds of thousands points. As such, the time to achieve convergence will increase with the size of the input cloud and may limit real-time response. Down-sampling of the input cloud reduces points and complexity for matching.

2) *Resolution of Reference Map*: In a similar way, the complexity of the map affects NDT matching performance. Resolution corresponds to the size of the ND voxels, a large resolution improves processing time but reduces features and so matching becomes unstable. On the other hand, very small resolution means higher processing time and causes incorrect associations between input cloud and very close ND voxels, therefore accuracy is affected.

3) *VoxelGrid Filter*: Similar to the map resolution, the voxel grid filter is a down-sampling method applied on the input scan. A 3D grid is created on the input cloud, the local cloud in a voxel is replaced by the centroid (for the fields of x , y , z and intensity). Voxel grid filter preserves the general coverage (in distance) of the input cloud and reduces noise, but does not preserve the ring structure: the centroid may correspond to a point in between two rings unrelated to the original scan. By reducing the input cloud complexity according to the voxel grid cell size, the number of iterations to achieve convergence may be reduced.

4) *Number of LiDAR Beams*: As show in Table I, there are multiple 3D LiDARs available for vehicle navigation, and one of their distinctive attributes is the number of beams (lasers or channels) and their distribution. A high number of beams and a fine horizontal resolution mean the size of the input pointcloud is large and thus more time is necessary

for processing. Finer vertical angular resolutions mean better estimation of the voxel grid vertical centroid.

5) *Matching Initialization*: It is important to define the initial position and pose before a matching cycle with new scan data. As the vehicle moves continuously over time, the position computed in the previous cycle is used as a guess for the new cycle. In addition, the use of dead reckoning such as speed, acceleration, odometry and other navigation systems such as IMU and GNSS, can help improve the estimation of the initial position before the next cycle.

III. MULTIPLE LiDAR DYNAMIC TRAFFIC DATA

A. Data Collection

The target was to collect data in a variety of traffic conditions, including different type of environments, varying density of traffic and times of the day. We drove our instrumented vehicle three times per day and collected data for the following key time periods:

- Morning (9am-10am)
 - Pedestrian traffic: medium-low
 - Vehicle traffic: high
 - Conditions: people commuting to work, university students and staff arriving on the campus. Clear to overcast weather.
- Noon (12pm-1pm)
 - Pedestrian traffic: high
 - Vehicle traffic: medium-low
 - Conditions: large number of university students and staff heading to and from the various cafeterias and restaurants around Campus. These are largely accessible by walking, so vehicle traffic is relatively low around this time. Clear to overcast weather.
- Afternoon (2pm-4pm)
 - Pedestrian traffic: low
 - Vehicle traffic: medium-low
 - Conditions: foot traffic around campus is low during this busy work and class period, and vehicle density is also relatively normal or low. Clear to overcast weather.

Fig. 1 shows the vehicle used for data capture. The 3D LiDAR on top was replaced for each experiment only after the three time periods were recorded, only one LiDAR was used at a time to avoid noise due to mutual interference. Data from other sensors (RGB camera, IR camera, 360° camera, event camera, IMU, GNSS, CAN) was also recorded together with LiDAR data, together with timestamps, using ROS[23]. In addition, we collected calibration data for each new LiDAR setup to perform extrinsic LiDAR to camera calibration, using a checkerboard and various other points of interest. Clear lighting conditions were ensured to record such data.

Fig. 2 shows the main trajectory followed to record dynamic traffic data. Our dataset also offers a reference pointcloud map, created by a professional mobile mapping system (MMS), and which includes 3D coordinates and RGB

data. Vector map files (HD map) for public road outside of the Nagoya University campus, are also provided.

B. Evaluation Routes

From the main trajectory shown in Fig. 2, we selected 3 different routes for this study:

- Route A (blue): about 749 m of private roads inside Nagoya University, narrow, surrounded by trees and buildings, gentle slopes; maximum velocity allowed inside the campus is 30 km/h.
- Route B (yellow): about 475 m of public urban roads surrounding Nagoya University campus, wide, multiple lanes, large intersections, traffic signs and marks, mostly flat; maximum velocities between 40 km/h to 50 km/h.
- Route C (green): about 797 m of public urban roads surrounding Nagoya University campus, two lanes, intersections, hilly (7.6% average slope); maximum velocity 40 km/h.

For each route, we used the previously recorded sensor LiDAR log data included as part of our LIBRE dataset. To keep relative consistency in driving conditions, we chose the morning time rides for this study. In total, thirty (ten LiDARs times 3 routes) different evaluations for 3D map creation and for vehicle localization.

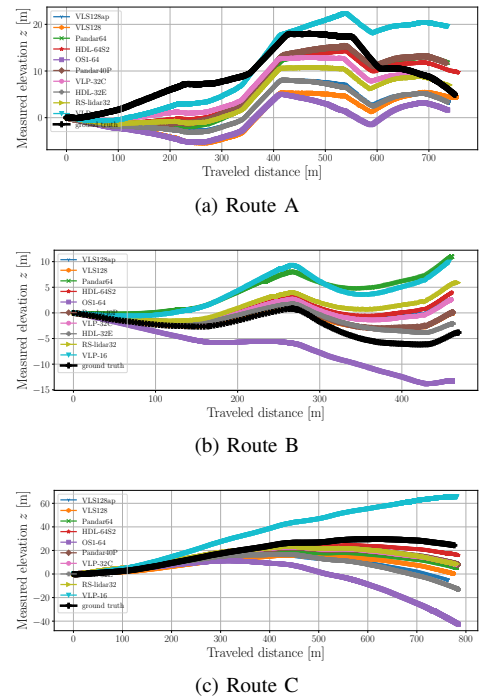


Fig. 3: Elevation errors due error accumulation during map creation.

IV. MAPPING EVALUATION

For each LiDAR and for each route, we created a 3D map using NDT for mapping implementation in Autoware. The NDT resolution was defined as 1 m, the maximum number of iterations to 50, the minimum range was 3 m and maximum range 200 m. To add new scans, especially during congested

	Sensor	Beams	N. points	Drive(s)	N. scans	Mean iter.	Std. iter.	Mean Fit.Sc.	Std. Fit.Sc.	MME	MPV
A	VLS128ap	128	160390220	204	1958	5.3805	8.3893	0.5175	0.0430		
	VLS128	128	126705326	160	1586	6.1513	8.4786	0.5453	0.0335	0.5701	0.4045
	Pandar64	64	134901915	158	1571	6.1948	10.1055	0.5154	0.0315		
	OS1-64	64	60912465	149	1486	4.3419	8.3900	0.5254	0.0304	0.5849	0.3851
	HDL-64S2	64	78402509	177	1764	5.9195	8.0350	0.5265	0.0481	0.2976	0.2900
	Pandar40P	40	81345147	153	1527	5.5200	8.7917	0.5262	0.0359	0.4923	0.3945
	VLP-32C	32	29679934	155	1528	3.1041	4.9624	0.5233	0.0379	0.4772	0.3867
	RS-lidar32	32	30053527	153	1505	4.0339	6.9112	0.5271	0.0404	0.5283	0.3944
	HDL-32E	32	35845160	155	1547	3.9774	6.9487	0.5236	0.0423	0.0299	0.2896
VLP-16	16	13215302	147	1447	2.3918	2.8995	0.5355	0.0406	0.4338	0.3823	
B	VLS128ap	128	93933095	145	1388	3.3927	5.3527	0.5398	0.0331	0.8185	0.4822
	VLS128	128	73962681	150	1494	3.2088	4.5320	0.5873	0.0244	0.6429	0.4347
	Pandar64	64	80049525	289	2901	2.4430	2.6135	0.5200	0.0231	0.5289	0.4500
	OS1-64	64	37105260	80	798	3.0727	6.0023	0.5328	0.0227	0.6937	0.4061
	HDL-64S2	64	44907042	93	924	5.0498	7.7395	0.5187	0.0313	0.4298	0.3357
	Pandar40P	40	46905632	148	1477	2.9255	4.6709	0.5224	0.0296	0.5788	0.4254
	VLP-32C	32	17055829	135	1345	2.4409	3.4703	0.5344	0.0341	0.5318	0.4150
	RS-lidar32	32	18378976	134	1318	2.6381	4.4722	0.5486	0.0325	0.5865	0.4215
	HDL-32E	32	20332647	72	716	3.3254	5.9123	0.5371	0.0362	0.2752	0.3340
VLP-16	16	7550326	128	1263	2.2486	2.8580	0.5372	0.0352	0.5446	0.4097	
C	VLS128ap	128	172433639	80	767	7.7405	13.0467	0.5626	0.0496		
	VLS128	128	118462134	90	895	6.0335	9.0134	0.6249	0.0447	0.5407	0.4506
	Pandar64	64	139121463	88	877	5.2201	8.8084	0.5391	0.0534		
	OS1-64	64	56799362	143	1427	2.5200	4.2354	0.5473	0.0341	0.6532	0.4188
	HDL-64S2	64	68186933	173	1723	3.8938	5.8987	0.5114	0.0495	0.4340	0.3401
	Pandar40P	40	71191899	96	957	4.3386	8.4673	0.5490	0.0535	0.5515	0.4615
	VLP-32C	32	29788546	87	866	3.1166	5.7595	0.5435	0.0688	0.4193	0.4281
	RS-lidar32	32	27233475	154	1515	2.5300	3.3160	0.5346	0.0564	0.4301	0.4106
	HDL-32E	32	28122526	94	936	3.0962	5.6704	0.5566	0.0482	0.2365	0.3502
VLP-16	16	15153288	257	2524	2.0959	0.9073	0.5216	0.0382	0.5298	0.4145	

TABLE II: Mapping results for each route and each LiDAR.

traffic, the minimum shift (translation) parameter was set to 1 m. After mapping the maps were not down-sampled to keep their integrity for this analysis, thus some of the maps are too large to be used for practical self-driving. The specs of the computer used in this evaluation are: Intel Xeon CPU E3-1545M with 4 cores/8 threads, NVIDIA Quadro M1000M GPU with 4GB GPU memory and 512 GPU cores, 32GB main RAM and a external 2TB SSD storage for log data recording.

Fig. 3 shows the elevation versus traveled distance for each LiDAR and each route while creating maps (ground truth is shown in black). Since each ride is slightly different (ex., changing lanes to avoid obstacles) the differences in trajectories in the XY plane are not considered here, instead the most important problem of drifting in elevation due to accumulated errors. While LiDARs with higher number of beams, finer vertical angular resolution, and higher range precision are closer to the ground truth, VLP-16 with lowest beam count and OS1-64 with lower range accuracy have the highest vertical errors. The reasons for this elevation error may be found on the NDT mapping algorithm itself, as reported previously in [24], and more research is necessary, however this work sheds light on the dependency of the LiDAR beams configuration. The environment may also play a role in such errors, routes B and C are regular roads while route A is a narrow road on the university campus.

We also consider as additional metrics to analyze map quality, the mean map entropy (MME) and the mean plane variance (MPV) discussed in Razlaw *et al.*[25]. The mean map entropy (MME) score $H(M)$ of map M is given by

Eq. 4 as:

$$h(\mathbf{x}_k) = \frac{1}{2} \ln |2\pi e \Sigma(\mathbf{x}_k)|$$

$$H(M) = \frac{1}{M} \sum_i^M h(\mathbf{x}_i) \quad (4)$$

The covariance $\Sigma(\mathbf{x}_k)$ of point \mathbf{x}_k is computed using a kd-tree neighborhood search with radius r . The mean plane variance (MPV) score $V(M)$ of the map is given by equation Eq. 5 as:

$$V(M) = \frac{1}{M} \sum_i^M v(\mathbf{x}_i) \quad (5)$$

where $v(\mathbf{x}_i)$ is the upper quartile of distances with the best fitting plane for the points around \mathbf{x}_k in the search radius r .

For the ground truth reference map provided by MMS, the MME score is 0.294893 and the MPV score is 0.669889. Table II summarizes the results during mapping³, including the number of points in each final map, the driving time for the route, number of scans included, and so on. As expected, LiDARs with higher number of beams take more time (iterations), while the fitness score remains similar for all sensors. The MME and MPV scores seem to favour the legacy sensors HDL-64S2 and HDL-32E, possibly due to the quality of their calibration and measurement accuracy when compared with newer devices.

One element which affects the MME and MPV scores is the presence of objects in the map, in particular on the road

³At the time of submission, missing MME and MPV values were being computed.

surface. Fig. 4 shows the reference MMS map colored by point entropy and point plane variance, both using a search radius r of 1 m. The map portion covered by vector maps was curated and no motion artifacts are observed, however map data inside the Nagoya University campus clearly show trails from objects in motion during mapping and not filtered here. The traffic conditions were slightly different while driving with each sensor, sometimes there were vehicles present leaving such trails on the map, and thus MME and MPV scores rose. Using the vector maps to filter road points and then removing points inside the road with high entropy and plane variance is a possible filtering strategy to consider.

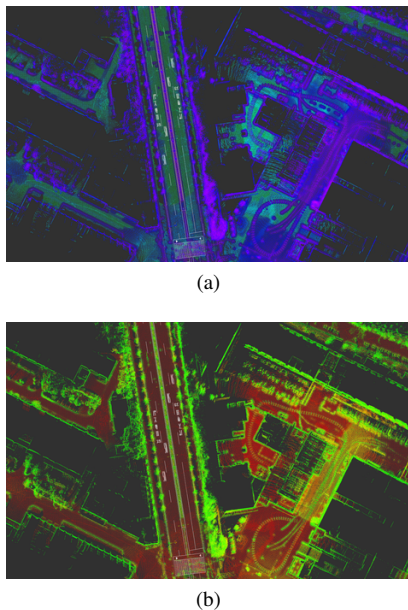


Fig. 4: Reference MMS map coloured entropy(a) (green lower entropy, magenta is higher entropy) and by plane variance (b) (red lower variance, green higher variance) for each point.

V. LOCALIZATION EVALUATION

We performed thirty experiments on localization, using the ground truth reference map, and NDT matching implementation in Autoware. NDT matching requires the input cloud to be down-sampled, we used the voxel grid filter with a voxel size of 2 m and the maximum distance of 200 m. Similar to NDT mapping, NDT resolution was set to 1 m, maximum number of iterations to 50, error threshold was 1 m. The initial position was manually defined for each case. Fig. 5 show qualitative results of the different LiDARs during localization at specific locations. These images show the achieved coverage by each LiDARs’s original input cloud after being transformed. Examples of filtered input cloud by the voxel grid filter are shown in Fig. 7.

Fig. 6 shows the localization performance of the different LiDARs per each route. In general, VLP-16 had a very fast convergence while the LiDARs with higher number of beams struggled. The higher iterations at the beginning are due to the different initialization configurations required for

each sensor and route. Route B shows the higher number of fluctuations in iterations, this is partially due to changes in the environment not included in the reference MMS map. Also, this route includes portions where maximum speed was 50 km/h, the higher speed and the constant 10 Hz scanning rate of the sensors points to the need of motion compensation in NDT.

VI. CONCLUSIONS

In this work, we presented a detailed comparison and characteristics of ten different 3D LiDARs, each one a different model from diverse manufacturers, for navigation tasks (3D mapping and 6-DOF localization), using as common reference the Normal Distributions Transform (NDT). We analyzed each LiDAR pointcloud data alone and without assistance of any other navigation and dead reckoning systems. Data in this study comes from dynamic traffic data in our LIBRE dataset.

While ultimate reason may lie in the NDT implementation, the elevation during mapping for all 3D LiDARs was incorrect in all cases, drifting in elevation due to accumulated errors in posture estimation, the LiDAR’s beams configuration and the surrounding environment seem to have an important effect. Correct localization was achieved for all LiDARs using a reference ground truth map. Even if all input clouds were equally filtered, the number of iterations varied largely especially for multiple beam configurations and also depending on the environment (existence of sufficient reference data).

Future directions derived from this work include, studying the elevation problem in NDT mapping, evaluation using other algorithms such as LeGo-LOAM[26], different down-sampling pre-processing filtering which preserves the point cloud structure, automatic tuning of localizer parameters. The application of MME based feature points for localization will be also considered.

ACKNOWLEDGMENTS

This work was supported by the Core Research for Evolutional Science and Technology (CREST) project of the Japan Science and Technology Agency (JST). We would like to extend our gratitude to the Autoware Foundation⁴ to realize this project. Finally, and as a matter of course, this work would not have been possible without the invaluable support of Velodyne Lidar Inc., Ouster Inc., Hesai Photonics Technology Co., Ltd., and RoboSense–Suteng Innovation Technology Co., Ltd.

REFERENCES

- [1] Velodyne LiDAR, Inc. Alpha Prime: Powering Safe Autonomy (63-9679 Rev-1). https://velodynelidar.com/wp-content/uploads/2019/12/63-9679_Rev-1_DATASHEET_ALPHA-PRIME_Web.pdf. [Accessed 20-January-2020].
- [2] ——. Alpha Puck: Ultra-High Resolution, Long Range Lidar for Autonomous Systems (63-9480 Rev-3). https://autonomoustuff.com/wp-content/uploads/2019/05/AlphaPuck_Datasheet_whitelabel.pdf. [Accessed 20-January-2020].

⁴<https://www.autoware.org>

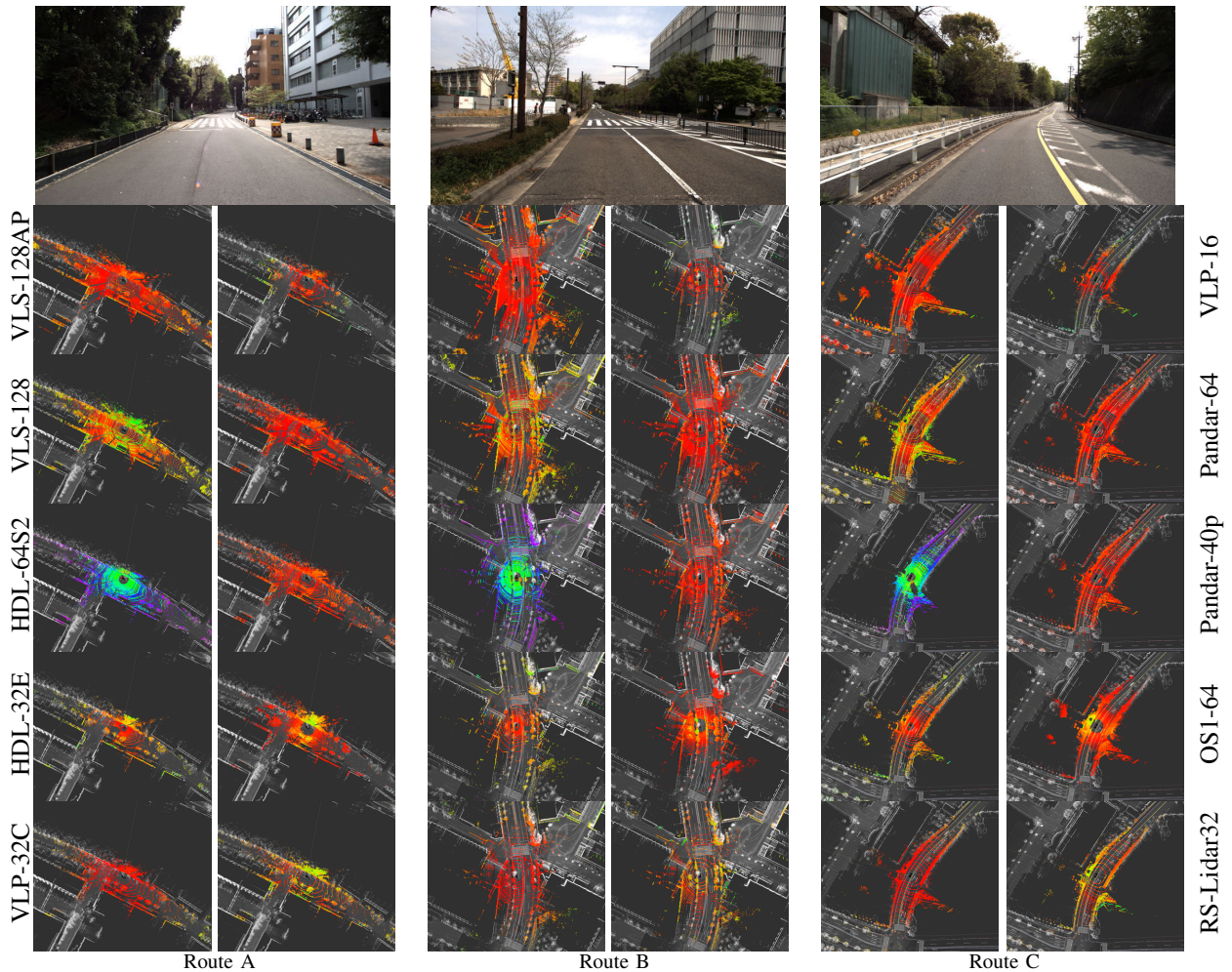


Fig. 5: Qualitative results of localization for each LiDAR for each LiDAR, grouped by route and colored by intensity (auto scaled), scenes of the chosen location are included. For each group, the LiDAR models are indicated by the given labels.

- [3] —. User's Manual and Programming Guide – HDL64-S2 and S2.1 (63HDL64E S2 Rev-F). <https://www.argocorp.com/cam/special/Velodyne/common/pdf/63-HDL64ES2g%20HDL-64E%20S2%20CD%20HDL-64E%20S2%20Users%20Manual%20low%20res.pdf>. [Accessed 20-January-2020].
- [4] —. HDL-32E: High Resolution Real-Time 3D Lidar Sensor (97-0038 Rev-N). https://velodynelidar.com/wp-content/uploads/2019/12/97-0038-Rev-N-97-0038-DATASHEETWEBHDL32E_Web.pdf. [Accessed 20-January-2020].
- [5] —. Ultra Puck: High Resolution Real-Time Lidar for Autonomous Systems (63-9378 Rev-F). https://velodynelidar.com/wp-content/uploads/2019/12/63-9378_Rev-F-Ultra-Puck_Datasheet_Web.pdf. [Accessed 20-January-2020].
- [6] —. Puck: Versatile Real-Time Lidar Sensor (63-9229 Rev-K). https://velodynelidar.com/wp-content/uploads/2019/12/63-9229_Rev-K-Puck_-_Datasheet_Web.pdf. [Accessed 20-January-2020].
- [7] Hesai Photonics Technology Co., Ltd. Pandar64: 40-Channel Mechanical LiDAR. https://web2019.azureedge.net/uploads/Pandar64_Brochure.pdf. [Accessed 20-January-2020].
- [8] —. Pandar40P: 40-Channel Mechanical LiDAR. https://web2019.azureedge.net/uploads/Pandar40P_Brochure.pdf. [Accessed 20-January-2020].
- [9] Ouster, Inc. OS1 Gen1 Datasheet. <http://data.ouster.io/downloads/OS1-gen1-lidar-sensor-datasheet.pdf>. [Accessed 20-January-2020].
- [10] Robosense–Suteng Innovation Technology Co., Ltd. RS-LiDAR-32 Brochure. <https://qncdn.sz-sti.com/RS-LiDAR-32%20Brochure%20EN%2020190820.pdf>. [Accessed 20-January-2020].
- [11] S. Thrun, "Robotic mapping: A survey," *Exploring artificial intelligence in the new millennium*, vol. 1, no. 1-35, p. 1, 2002.
- [12] S. Thrun, M. Montemerlo, H. Dahlkamp, D. Stavens, A. Aron, J. Diebel, P. Fong, J. Gale, M. Halpenny, G. Hoffmann *et al.*, "Stanley: The robot that won the DARPA Grand Challenge," *Journal of Field Robotics*, vol. 23, no. 9, pp. 661–692, 2006.
- [13] Yole Développement. The automotive LiDAR market. http://www.woodsdecap.com/wp-content/uploads/2018/04/Yole-WCP-LiDAR-Report_April-2018-FINAL.pdf. [Accessed 10-January-2020].
- [14] Nagoya University and TierIV. LIBRE: LiDAR Benchmark Reference dataset. <https://sites.google.com/g.sp.m.is.nagoya-u.ac.jp/libre-dataset>. [Accessed 20-February-2020].
- [15] A. Carballo, J. Lambert, A. Monrroy, D. Wong, P. Narksri, Y. Kitsukawa, E. Takeuchi, S. Kato, and K. Takeda, "LIBRE: The multiple 3d lidar dataset," *arXiv preprint arXiv:2003.06129*, 2020, (accepted for presentation at IV2020).
- [16] E. Takeuchi and T. Tsubouchi, "A 3-d scan matching using improved 3-d normal distributions transform for mobile robotic mapping," in *Proceedings of the IEEE/RSJ International Conference on Intelligent Robots and Systems (IROS)*. IEEE, 2006, pp. 3068–3073.
- [17] M. Magnusson, A. Lilienthal, and T. Duckett, "Scan registration for autonomous mining vehicles using 3D-NDT," *Journal of Field Robotics*, vol. 24, no. 10, pp. 803–827, 2007. [Online]. Available: <http://dx.doi.org/10.1002/rob.20204>
- [18] M. Magnusson, "The three-dimensional normal-distributions transform: an efficient representation for registration, surface analysis, and loop detection," PhD dissertation, Örebro Universitet, 2009.
- [19] Autoware Foundation. Autoware-AI. <https://gitlab.com/autowarefoundation/autoware.ai>. [Accessed 20-February-2020].
- [20] S. Kato, S. Tokunaga, Y. Maruyama, S. Maeda, M. Hirabayashi, Y. Kitsukawa, A. Monrroy, T. Ando, Y. Fujii, and T. Azumi, "Autoware

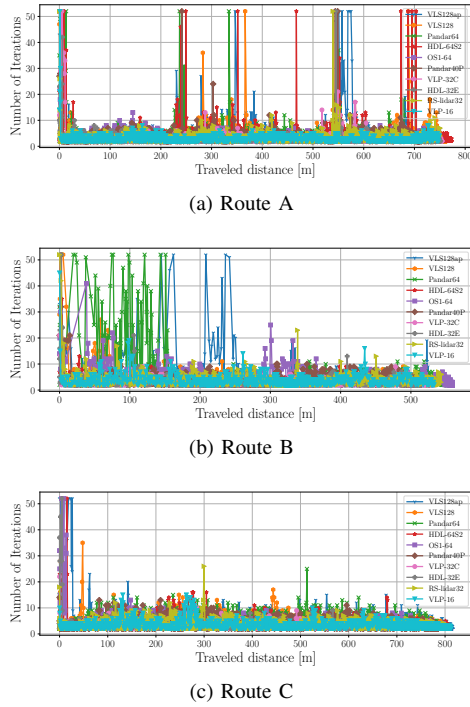


Fig. 6: Number of iterations per LiDAR and per route.

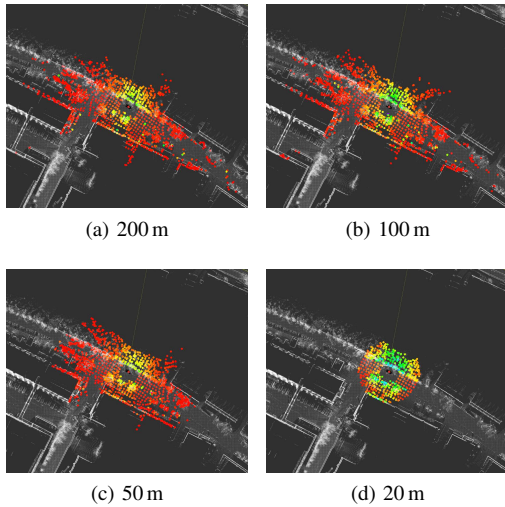


Fig. 7: Voxel grid filter applied to the OS1-64 pointcloud with different maximum range filters.

on board: Enabling autonomous vehicles with embedded systems,” in *ACM/IEEE International Conference on Cyber-Physical Systems (ICCP)*. IEEE, 2018, pp. 287–296.

- [21] P. Biber and W. Straßer, “The normal distributions transform: A new approach to laser scan matching,” in *Proceedings of the IEEE/RSJ International Conference on Intelligent Robots and Systems (IROS)*, vol. 3. IEEE, 2003, pp. 2743–2748.
- [22] H. Sobreira, C. M. Costa, I. Sousa, L. Rocha, J. Lima, P. Farias, P. Costa, and A. P. Moreira, “Map-matching algorithms for robot self-localization: a comparison between perfect match, iterative closest point and normal distributions transform,” *Journal of Intelligent & Robotic Systems*, vol. 93, no. 3-4, pp. 533–546, 2019.
- [23] M. Quigley, B. Gerkey, K. Conley, J. Faust, T. Foote, J. Leibs, E. Berger, R. Wheeler, and A. Ng, “ROS: an open-source robot operating system,” in *IEEE International Conference on Robotics and Automation (ICRA) Workshop on Open Source Robotics*, Kobe, Japan, May 2009.
- [24] A. Carballo, S. Seiya, J. Lambert, H. Darweesh, P. Narksri, L. Y.

Morales, N. Akai, E. Takeuchi, and K. Takeda, “End-to-end autonomous mobile robot navigation with model-based system support,” *Journal of Robotics and Mechatronics*, vol. 30, no. 4, pp. 563–583, 2018.

- [25] J. Razlaw, D. Droschel, D. Holz, and S. Behnke, “Evaluation of registration methods for sparse 3d laser scans,” in *2015 European Conference on Mobile Robots (ECMR)*. IEEE, 2015, pp. 1–7.
- [26] T. Shan and B. Englot, “LeGO-LOAM: Lightweight and ground-optimized lidar odometry and mapping on variable terrain,” in *Proceedings of the IEEE/RSJ International Conference on Intelligent Robots and Systems (IROS)*. IEEE, 2018, pp. 4758–4765.